Spatial Variations in Silicate-to-Nitrate Ratios in the Southern Ocean Surface Waters are Controlled in the Short Term by Physics Rather Than Biology

Pieter Demuynck[1], Toby Tyrrell[1], Alberto Naveira Garabato[1], Mark C. Moore[1], and Adrian P. Martin[2]

[1]Ocean and Earth Science, University of Southampton, Southampton SO14 3ZH, UK
[2]National Oceanography Centre, Southampton SO14 3ZH, UK

Correspondence: Pieter Demuynck (pd1n18@soton.ac.uk)

Abstract. The nutrient composition (high in nitrate but low in silicate) of Subantarctic Mode Water (SAMW) forces diatom scarcity across much of the global surface ocean. This is because diatoms cannot grow without silicate. After formation and downwelling at the Southern Ocean's northern edge, SAMW re-emerges into the surface layers of the mid- and low-latitude oceans, providing a major nutrient source to primary producers in those regions. The distinctive nutrient composition of SAMW

5   originates in the surface waters of the Southern Ocean, from which SAMW is formed. These waters are observed to transition from being rich in both silicate and nitrate in high-latitude areas of the Southern Ocean, to being nitrate-rich but silicate-depleted in SAMW formation sites further north. Here we investigate the key controls of this change in nutrient composition with an idealised model, consisting of a chain of boxes linked by a residual (Ekman- and eddy-induced) overturning circulation. Biological processes are modelled on the basis of seasonal plankton bloom dynamics, and physical processes are modelled

10   using a synthesis of outputs from the data-assimilative Southern Ocean State Estimate. Thus, as surface water flows northward across the Southern Ocean toward sites of SAMW formation, it is exposed in the model (as in reality) to seasonal cycles of both biology and physics. Our results challenge previous characterisations of the abrupt northward reduction in silicate-to-nitrate ratios in Southern Ocean surface waters as being predominantly driven by biological processes. Instead, our model indicates that, over shorter timescales (years to decades), physical processes connecting the deep and surface waters of the Southern

15   Ocean (i.e. upwelling and entrainment) exert the primary control on the spatial distribution of surface nutrient ratios.

1   Introduction

20   The Southern Ocean (SO) is an important component of the Earth system in its own right, but also through the influence it exerts over a large fraction of the rest of the ocean through nutrient supply. It was hypothesised (Sarmiento et al., 2004), and is

now generally accepted, that Subantarctic Mode Water (SAMW, see Figure 2) acts as a conduit carrying nutrients from the SO to the mid- and low-latitude oceans, thus controlling the productivity of those regions. SAMW flows along the global ocean thermocline (at depths of 100 - 500 m, ($\sigma - \theta \sim 26.8$), and supplies the surface layers with nutrients via upwelling centers such as e.g., equatorial Pacific and off South America (Sarmiento et al., 2004). Global ocean model runs in which SAMW is

5   artificially altered to contain no nutrients lead to up to a four-fold reduction in primary production outside the SO (Sarmiento et al., 2004; Palter et al., 2010). A range of biogeochemical processes in the upper limb (Fig. 2) of the SO overturning circulation modify the water properties of surface waters subducting in the SAMW formation sites. Properties acquired by these water during their time at the surface in the SO thus exert an important influence on the biogeochemistry of many upwelling regions elsewhere in the global ocean.

10   An important feature of the SO overturning's upper limb is the meridional gradient of surface nutrient concentrations, with highest values in the south and a northward reduction in nutrient levels. The gradient is most substantial for silicate: from more than 50 $mmol\,m^{-3}$ at the high-latitude winter-ice boundary, to 10 $mmol\,m^{-3}$ and less at the Polar Front, according to observations (Tréguer and Jacques, 1992). A similar decline was observed along a 42°E section, with marked steps in nutrient concentrations at each SO front (Pollard et al., 2002). Assmy et al. (2013) reported decreases of Si from 70 $mmol\,m^{-3}$ in

15   the upwelling waters to less than 5 $mmol\,m^{-3}$ north of the Polar Front. Along that same transect, nitrate concentrations only decreased from about 30 $mmol\,m^{-3}$ to 23 $mmol\,m^{-3}$. In the Southern Ocean component of the United States Southern Ocean Joint Global Ocean Flux Study (JGOFS), AESOPS (Antarctic Environment and Southern Ocean Process Study) performed several cruises along a transect at 170°W. During those cruises (in Oct. 1997, Nov. 1997, Dec. 1997, Jan. 1998 and Feb. 1998) significant gradients in macronutrients were observed: nitrate concentration of about 25 - 30 $mmol\,m^{-3}$ at 68°S to 15

20    $mmol\,m^{-3}$ at 50°S and silicate concentrations decreased from 60 - 70 $mmol\,m^{-3}$ at 68°S to 0-10 $mmol\,m^{-3}$ at 50°S (Smith et al., 2000). Fig. 1 shows surface nitrate and silicate as observed during a German SO JGOFS cruise along a section at 5°E (Read et al., 2002). The gradients and the difference between silicate and nitrate are clear. This feature, present in all sectors of the SO, has important consequences for ocean biogeochemistry on a global scale. As a result of the residual surface nitrate in mode water formation areas, a considerable amount of nitrate is subducted into SAMW and Antarctic Intermediate Water. The

25   depleted levels of silicate in the subduction regions leads to a relatively modest amount of silicate being exported from the SO, hence preventing diatom blooms in nitrate-rich but silicate-poor regions of the global ocean (Assmy et al., 2013).

   The central question addressed in this paper is why the surface waters that subduct to form SAMW are depleted in silicate but not nitrate. It is not immediately obvious why this should be. According to the simplified view shown in Fig. 2, Circumpolar Deep Water (CDW) upwells at the Southern Boundary of the Antarctic Circumpolar Current (ACC) to provide surface closure

30   of the SO overturning's upper limb. CDW has a higher concentration of silicate than nitrate (50 - 70 and 20-30 $mmol\,m^{-3}$, respectively), as do surface waters near the Southern Boundary. Diatoms at a variety of locations around the world typically take up silicate and nitrate in a ratio close to 1:1 (Brzezinski, 1985), and therefore it might be expected that, if removal by diatoms is the primary biogeochemical process in operation, that nitrate would run out before silicate rather than the opposite.

   The preferential removal of silicate to nitrate in SO surface waters is generally attributed to biological processes, for two

35   reasons. First, it has long been known that diatoms in the SO are hypersilicified. These diatoms have unusually thick frustules,
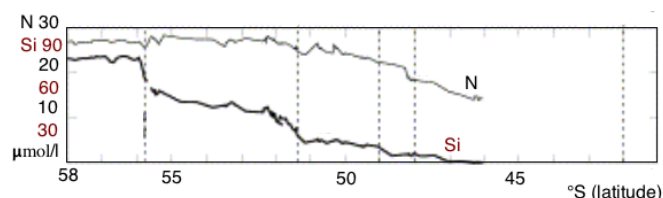
Figure 1. Nitrate and silicate concentration in the surface layer observed during a German SO JGOFS cruise along 5°E, Figure modified from Pollard et al. (2002)

and their Si:N ratios of diatoms often greatly exceed 1:1 (Brzezinski et al., 2002), possibly in response to the iron limitation that prevails in the SO, although according to Timmermans et al. (2004) SO diatoms are hypersilicified in the absence of iron stress as well. Iron stress tends to increase the Si:N ratio observed in diatom species from an average of 1:1 to values higher than 4:1, and may thus partly explain the stronger depletion of Si than N (Assmy et al., 2013). Second, N and Si export are

5 thought to be uncoupled (Tréguer and Jacques, 1992; Pollard et al., 2002; Assmy et al., 2013), in the sense that particulate Si (diatom frustules) sinks relatively fast and either dissolves at great depth or does not dissolve, ending up in the siliceous ooze (Assmy et al., 2013). A modelling study by Holzer et al. (2014) showed that the average phosphate regeneration depth is ± 600 m, whereas the corresponding mean depth of silicate regeneration in the SO is ± 2300 m. Silicate that remineralises in the CDW is transported back southwards at depth, and re-surfaces near the Southern Boundary. Thus, silicate ends up in a

10 vertical recycling loop, and becomes efficiently trapped. Further, remineralisation of nitrate and silicate is different, as bacteria are very efficient at decomposing organic nitrogen in relatively shallow layers. This results in a significant proportion of the nitrogen demand being provided by efficient bacterial recycling of organic nitrogen, leading, on occasion, to mass sinking of empty diatom frustules with no organic matter left inside them (Assmy et al., 2013). Almost half of the global Si inventory goes through a SO-to-SO loop (Holzer et al., 2014). While phosphate (similar to nitrate), last used in the SO has only a 56%

15 probability of reemerging in the SO photic zone and of being used in the SO again, the probability for SO silicate being used in the SO again is as high as 95% (Holzer et al., 2014).

In this paper, we assess the controls of the meridional gradient in Si-to-N ratios characteristic of the SO with an idealised model representing all of the region's important physical and biological processes. Our results highlight the pivotal role of physical processes in sustaining the nutrient distribution, on timescales up to decadal.

20 ## 2 Model Description

2.1 Physical model

The vertical partitioning of the model is based on observed seasonal changes in water mass properties along a section in Drake passage (Evans et al., 2014). In winter, strong surface cooling and wind-driven mixing between the deepening surface layer
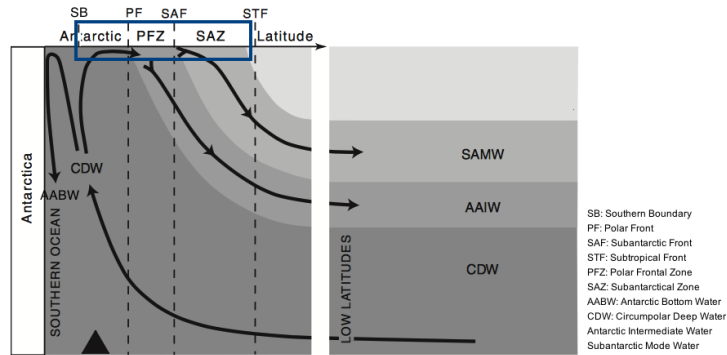
Figure 2. Circulation of main water masses in the Southern Ocean, Figure modified from Anderson et al. (2009). The box marks the region of interest
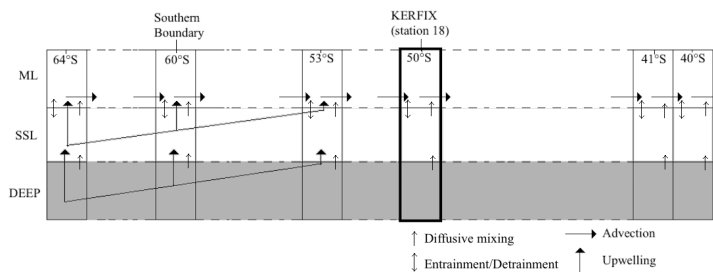
Figure 3. Structure of physical model: 1 box model contains a ML and a SSL. Northward advection in the ML connects the boxes in the meridional direction

and the underlying Antarctic Winter Water (AAWW) form a thick AAWW layer extending up to the surface. During summer, the upper part of AAWW is eroded by surface warming and internal mixing, and AAWW becomes a layer below a relatively shallow surface layer. The basic building block of the model is a 1-D box model in which the water column is divided into a mixed layer (ML) and a subsurface layer (SSL). The depth of the boundary condition at a certain latitude is defined as the

5   thickest ML rounded up to the nearest 100 m (See Table 1). The lower boundary of the SSL is fixed in depth at a certain latitude. Model boundary conditions are applied at this boundary, representing properties (assumed constant over time) of deep water beneath the SSL. In the model, the depth of the SSL is calculated as the difference between the depth of the fixed boundary and the ML depth. In summer, the ML is thin and the SSL is relatively thick, and vice versa in winter.

Table 1. Lower boundary of SSL per station in m below water surface

Station	1	2	3	4	5	6	7	8	9	10	11	12	13	14	15
Depth [m]	200	200	300	400	400	400	400	400	400	400	400	400	400	300	300
Station	16	17	18	19	20	21	22	23	24	25	26	27	28	29	30
Depth [m]	300	300	300	300	300	300	500	500	500	500	200	200	200	200	200

Starting at the Southern Boundary ($\sim$60°S) surface waters will move northward with a characteristic velocity of order 0.3 - 0.4 $km\,d^{-1}$, and eastward with a characteristic velocity of order 20 $km\,d^{-1}$ (Merlivat et al., 2015). In our work, the emphasis is on the northward flow of the water and processes affecting water properties following this flow. It is thus necessary for the model to span the region meridionally from the Southern Boundary ($\sim$60°S) to the latitude at which surface waters subduct

5 near the Subtropical Front (somewhere between 45°S and 30°S depending on longitude). 30 stations between 65°S and 40°S are included in the model. Each station is represented by a 1-D biogeochemical box model containing a SSL and a ML. While the intense eastward flow and the zonal connectivity of the SO would suggest that zonal advection should be included in the model, we omit the zonal dimension of the circulation here to preserve model simplicity. We choose to define our meridional section at 67°E to allow results to be compared to data from the KERFIX time series site.

10 Northward advection is induced by the strong and persistent wind (predominantly westerlies) over the Southern Ocean. In his summative paper, Deacon (1982) defines the Antarctic Divergence as the transition between easterlies and westerlies (situated between 62°S and 72°S). It is an Ekman divergence zone, in which circumpolar deep water reaches the surface and flows both north- and southwards. This upwelling is a prevalent over an extensive latitudinal range. As such, our model should include both upwelling and northward advection over a substantial latitudinal band north of the Southern Boundary.

15 Interaction between the ML and the SSL at a station is represented via diffusive mixing. Mixing is defined here as the tendency to homogenise water properties exhibiting a spatial gradient. Advection (including upwelling) and diffusion of a chemical concentration C are mathematically described by the well-known advection-diffusion equation:

$$\frac{\partial C}{\partial t} = D\,\bigtriangledown^2 C - \boldsymbol{v} \cdot \bigtriangledown C \tag{1}$$

Written out, this becomes:

20 $$\frac{\partial C}{\partial t} = D_x \frac{\partial^2 C}{\partial x^2} + D_y \frac{\partial^2 C}{\partial y^2} + D_z \frac{\partial^2 C}{\partial z^2} - v_x \frac{\partial C}{\partial x} - v_y \frac{\partial C}{\partial y} - v_z \frac{\partial C}{\partial z} \tag{2}$$

The first three terms of the equation describe diffusion with D denoting the diffusion coefficient along a certain axis and assumed constant. The last three terms describe advection. It is not easy to determine the value of D. Generally, horizontal diffusivity is assumed to be larger than vertical diffusivity by a factor of 10^7 (Garrett, 1979). The northward advective velocity v_x is about 5000 times larger than the upwelling velocity v_z. This suggests that horizontal diffusion may be more important

25 relative to horizontal advection than vertical diffusion relative to vertical advection. However, the tracer concentration gradient will be larger in the vertical direction than in the horizontal direction. We will assume that horizontal diffusion is of minor

importance compared to horizontal advection, as the diffusive term entails the calculation of the second derivative of a variable which will be an order of magnitude smaller than a first derivative featuring in the advective term. Horizontal diffusion will thus be omitted. In turn, vertical diffusion will be included in the model in a simplified form that is often adopted in simple box models. Meridional advection and upwelling will also be included in the model. Equation 2 then becomes:

$$\frac{\partial C}{\partial t} = D_z \frac{\partial^2 C}{\partial z^2} - v_x \frac{\partial C}{\partial x} - v_z \frac{\partial C}{\partial z} \qquad (3)$$

In the model, upwelling is made to take place in the first 15 stations. Q_{upw}, the vertical transport of water, decreases from $8650\,m^3/day$ at 63.52°S (calculated as the product of the estimated upwelling velocity at that latitude (Morrison et al., 2015) with the horizontal area of the box) to zero at 53.11°S. Vertical transport from the SSL to the ML is the same as from the deep layer to the SSL. Conservation of mass enables the calculation of the horizontal transport into ($Q_{adv,in}$) and out of ($Q_{adv,out}$) the ML in a box i. Note that horizontal transport is limited to the ML; there is no horizontal transport in the SSL. This is justified by the fact that Ekman flows typically extend to depths of about 50 - 100 m (Talley et al., 2011). Upwelling and advection of nutrients can now be calculated using $-v_x \frac{\partial C}{\partial x} - v_z \frac{\partial C}{\partial z}$ (see Eq. 3).

Fig. 3 is a representation of the physical structure of the box models and how they are linked together via advection and upwelling. For biogeochemical and physical processes happening within one box model please see Fig. 4.

In the box model a vertical gradient of a variable $\frac{\partial C}{\partial z}$ is established between the deep layer, the SSL and the ML. The diffusive flux of a variable C from a layer i+1 to the layer i above $D_z \frac{\partial^2 C}{\partial z^2}$ is simplified as:

$$F_{diff} = \frac{k_{mix}}{h}\left(C_{i+1} - C_i\right) \qquad (4)$$

where h is the ML or the SSL thickness. k_{mix} is the mixing coefficient set to $0.1\,m/day$.

Each model variable is subject to entrainment and detrainment. Entrainment is a process changing the concentration of a tracer due to an increase in the ML depth (this is called winter mixing in the model study by Pondaven et al. (2000), but for the sake of clarity, it is termed entrainment here). If the ML deepens in winter, water with a different concentration enters the ML. Note that entrainment only occurs when the ML deepens. When the ML shoals, the concentration of a tracer within the ML remains unchanged, but the concentration in the SSL changes. This process is called detrainment. Entrainment changes the concentration of a variable C as:

$$C_{ML+} = \frac{\Delta MLD \times C_{SSL} + MLD \times C_{ML}}{MLD + \Delta MLD} \qquad (5)$$

ΔMLD is the increase in the ML depth. C_{ML+} is the tracer concentration after entrainment; and C_{ML} is C in the ML before entrainment. Detrainment changes the concentration of a variable C as:

$$C_{SSL+} = \frac{\Delta MLD \times C_{MLD} + SSLD \times C_{SSL}}{SSLD + \Delta MLD} \qquad (6)$$

ΔMLD is the reduction in the ML depth. C_{SSL+} is the variable after detrainment; C_{SSL} is C in the subsurface layer before detrainment.

2.2 Biogeochemical model

Cycling of N, Si and Fe in the ML and the SSL are modeled through a simplified food web, and through interaction between the layers and interaction with the boundary conditions (Fig. 4). The ecosystem model is also forced by changes in the ML depth and in solar irradiance, which both affect the photosynthetically active radiation (PAR). The model contains a limited

5 number of state variables. In the ML: diatoms (D), nano- (and micro-) phytoplankton (P_f) and coccolithophores (P_c) represent the phytoplankton community; microzooplankton (Z) and mesozooplankton (MZ) represent the zooplankton community. In the ML and in the SSL, nitrate (N, N^*), silicate (Si, Si^*) and iron (Fe, Fe^*) are present. Two classes of detritus are defined in the ML and the SSL (Dt_N, Dt_N^*) and (Dt_{Si}, Dt_{Si}^*). Variables with a * are SSL variables. Nitrate has units of $mmol\,N\,m^{-3}$, silicate has units of $mmol\,Si\,m^{-3}$ and iron has units of $\mu mol\,Fe\,m^{-3}$. All other state variables except the silicate detritus pool

10 Dt_{Si}^* have units of $mmol\,N\,m^{-3}$.

2.2.1 Phytoplankton growth rate

Smaller pico- and nanophytoplankton species are dominant throughout the year in the SO (Smetacek et al., 2004). Increased biomass levels compared to this small background concentration are due to blooms of larger phytoplankton species, mainly diatoms (Smetacek et al., 2004). The biological part of the model contains only three phytoplankton species: diatoms, nano-

15 (and micro-) phytoplankton and coccolithophores. Nanophytoplankton and coccolithophores are grazed by microzooplankton. Microzooplankton and diatoms are a food source for mesozooplankton. Each phytoplankton species i has a reduced growth rate μ_i calculated as $\mu_i = \mu_{max,i} \times \phi \times \psi$ (Tyrrell and Taylor, 1996). ψ is a light limitation factor. The light limitation factor ψ has a Michaelis-Menten shape and is calculated as (Tyrrell and Taylor, 1996):

$$\psi = \frac{1}{30} \sum_{i=1}^{30} \left(\frac{I_z}{I_z + I_h} \right) \tag{7}$$

20 The ML is subdivided into 30 equal layers. At each depth $z = (i - 0.5) \times MLD/30$ the light intensity I_z is calculated. At each of the 30 layers ψ is computed. An averaged value of ψ over the ML is used.

About 50% (the infrared component) of surface solar radiation (I_{surf}) never penetrates to any great depth. Properties of the remaining 50% are highly dependent on the wavelength. It is common to use averaged light characteristics. However, a distinction is made between deeply penetrating green light and much less deeply penetrating red light. The light intensity at a

25 certain depth z is calculated as (Taylor et al., 1991):

$$I_z = 0.25 I_{surf} e^{-k_r z} + 0.25 I_{surf} e^{-k_g z} \tag{8}$$

k_r and k_g are the extinction coefficients for red and green light repectively.

ϕ is a nutrient limitation factor using Michaelis-Menten calculated as:

$$\phi = min \left(\frac{N}{N + N_{h,i}}, \frac{Si}{Si + Si_{h,i}}, \frac{Fe}{Fe + Fe_{h,i}} \right) \tag{9}$$
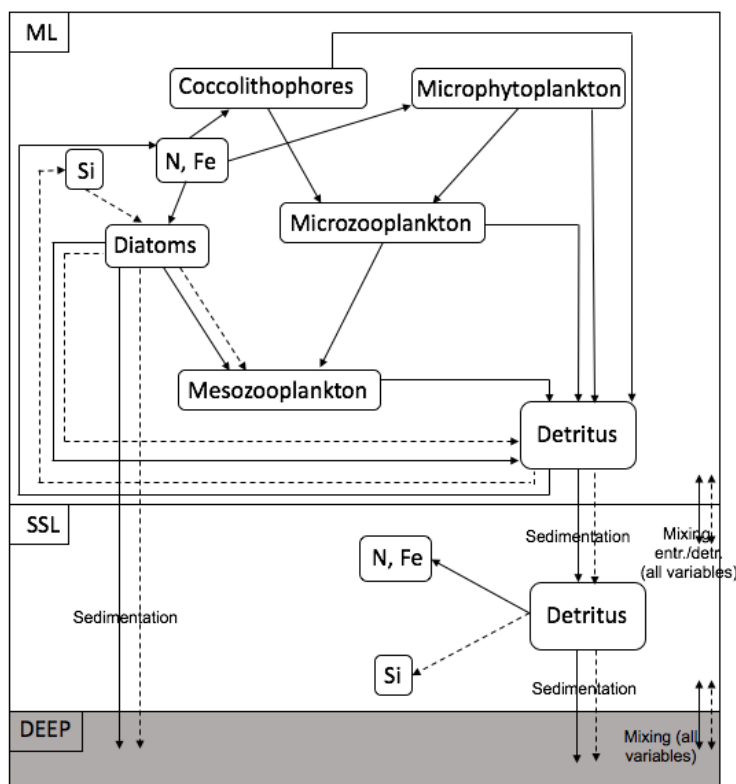
Figure 4. Structure of the ecosystem within one box model. The full arrows represent the flow of nitrogen and iron, the dashed arrows represent the flow of silicate

2.2.2 Phytoplankton stoichiometry

Phytoplankton and zooplankton are modelled in units of $mmol\,N\,m^{-3}$. In order to quantify the effect of biology on other variables like Fe and Si, it is necessary to know the stoichiometry of the phytoplankton. Because of the critical role of iron, it is important to use a realistic nitrate to iron ratio (extended Redfield ratio). The Southern Ocean Iron Experiments (SOFeX)

5 (2002-2003) (Twining et al., 2004) investigated the element stoichiometry of individual plankton cells before and after iron fertilisation. Before fertilisation the N:Fe ratio within diatoms was about 23 000; in flagellates it was similar. After fertilisation the ratio had decreased to about 7500. This suggests that phytoplankton use relatively more iron when it is widely available. Analysis of an algal culture revealed N:Fe ratio's of 4000 in diatoms and 2000 in flagellates (Ho et al., 2003). The variation is

considerable and it is a crude assumption to assume a constant N:Fe ratio. Thus, the N:Fe ratio is parameterised as:

$$N:Fe = 26000 - \frac{23500 \times Fe}{1.2} \tag{10}$$

where Fe denotes the iron concentration in $\mu mol\,m^{-3}$. The N:Fe ratio ranges between 15800:1 and 25900:1. The ratio is rather high, but iron is considered a limiting nutrient in vast areas of the SO (Martin et al., 1990), such that these high values are

5 justified. Equally important is the Si:N ratio. It is thought to depend on iron availability, with higher silicification when iron is scarce (Smetacek et al., 2004). Ratios higher than 4:1 have been recorded in *Fragilariopsis Kerguelensis* (Assmy et al., 2013; Timmermans et al., 2004). As in the model study by Pasquer et al. (2015) a parameterisation for the Si:N ratio will be used:

$$Si:N = 4 - \frac{3 \times Fe}{1.2} \tag{11}$$

where Fe again indicates the iron concentration in $\mu mol\,m^{-3}$. The ratio is restricted to values between 1 and 4.

10 ### 2.2.3 Model parameters

Model parameters are chosen within reasonable boundaries, based on literature (Oguz and Merico, 2006; Merico et al., 2006, 2004; Pondaven et al., 2000; Fasham, 1995; Pondaven et al., 1998; Taylor and Joint, 1990; Taylor et al., 1991, 1993). The phytoplankton mortality rate is constant. Grazing rates and grazing preference depend on absolute values of the prey biomass according to Pondaven et al. (2000). Diatoms can sink out of the ML because they form thick Si frustules. For that reason,

15 Si remineralisation is slower than that of N and Fe. Attached and free coccoliths are represented in the model following to (Merico et al., 2006) or (Tyrrell and Taylor, 1996). We refer to Table 2.

2.3 Numerical implementation

Each station has two active layers: the ML and the SSL. A meridional section from 65°S to 40°S is defined with 30 stations, resulting in a meridional resolution of less than 1°. The model time step is $\Delta t = 10$ min. The rate of change of a certain state

20 variable per m^3 is calculated using the forward Euler method. The simulation runs from 2 January 2008 to 30 December 2012. The temporal resolution of the model forcing is 3 days. The results of a 25-year simulation with cycled 5-year forcing are used as initial conditions for the final model run. For a full description of the model equations see Appendix A.

3 Overview of the datasets

3.1 Boundary conditions

25 The boundary conditions for the model are defined at the base of the SSL of each station along the meridional section. Boundary conditions are only required for nutrients, and they are fixed in time and space. The Global Ocean Data Analysis Project version 2 (GLODAPv2) (Olsen et al., 2016) contains data of about one million seawater samples from all over the worlds ocean, collected during almost 800 cruises between 1972 and 2013. The boundary conditions for Si and N at a specific station are

obtained by averaging all available data in a zonal band from 20°E and 120°E, 50° to the east and to the west of the KERFIX longitude (Fig. 5 (a) and 5 (b)). GLODAPv2 does not contain iron data. Iron is a critical variable when investigating the SO. Therefore, it is important to use good quality data. Two datasets are combined.The Tagliabue et al. (2012) dataset contains Fe measurements across the global oceans from the years 1978 - 2009. The GEOTRACES first intermediate data product is a

5   platform providing data from cruises around the world (Mawji and et al., 2015). The iron bottle data collected during 7 different cruises in the SO (GIPY06, GIPY05, GIPY04, GIPY02, GI04, GA02, GPpr02) provide 3216 sample points collected between 2007 and 2011. To define the iron boundary condition, the available data are averaged over the entire zonal band (Fig. 5 (c)). The boundary conditions are specified with a limited amount of data collected all over the open SO over a large timespan. The zonal and temporal dimension of the boundary conditions have therefore no meaning in the model.

10   ## 3.2 Model forcing

The Biogeochemical Southern Ocean State Estimation (B-SOSE) dataset (Verdy and Mazloff, 2016) is used for the model forcing (available at *http://sose.ucsd.edu*). B-SOSE is a model-generated best fit to SO observations - an observationally con-strained solution to the MIT general circulation model. It has a horizontal resolution of $1/6°$. Observations used in B-SOSE include Argo profiles, CTD measurements, mooring data, satellite measurements, etc. As it is observation-based, the results are

15   more uncertain in regions with limited observational coverage (Mazloff and National Center for Atmospheric Research Staff, 2016). The B-SOSE simulation provides data from 2 January 2008 to 30 December 2012 with a temporal resolution of 3 days. This resolution makes this dataset suitable for model forcing. The biological part of the model is forced with a regular seasonal cycle, specifically with seasonal variations in the ML depth and in solar irradiance. A property difference-based criterion will be used to define the ML depth (de Boyer Montégut et al., 2004). Often a temperature based criterion, $\Delta T = 0.2°C$ or a density

20   based criterion $\Delta \rho = 0.03 \, kg \, m^{-3}$ is chosen. In our model the $\Delta \rho = 0.03 \, kg \, m^{-3}$ density criterion is applied to the B-SOSE dataset. While the boundary conditions are an average in the zonal direction, the ML is defined at 30 stations between 65°S and 40°S at 67°E, a longitude which is close to the KERFIX time-series station. The daily averaged solar irradiance at the surface is calculated from the position of the sun as a function of day of year and latitude (Kirk, 1994). Cloud cover data is obtained from the NCEP/NCAR 40-year reanalysis project (Kalnay et al., 1996). Daily long-term average values over 40 years are used,

25   and hence cloud cover is representative of an average year. As a result of this, the solar irradiance forcing in the model is the same for each year. Highest irradiance is found in January, lowest in July

3.3 KERFIX timeseries

The KERFIX station is located in the SO at 50°40'S, 68°25'E, south of the Polar Front and southwest of the Kerguelen Islands. Temperature, salinity and oxygen were measured between January 1990 and March 1995. Nutrients and chlorophyll

30   data are available for the period January 1992 - December 1994. The frequency of sampling was once per month. The KERFIX program was the first 'offshore' program for regular multi-year acquisition of data in the SO (Jeandel et al., 1998). An important motivation for the KERFIX program was to increase the understanding of processes that control primary production in the area, which is rather low despite the high nutrient availability (Jeandel et al., 1998). The KERFIX site is considered a representative
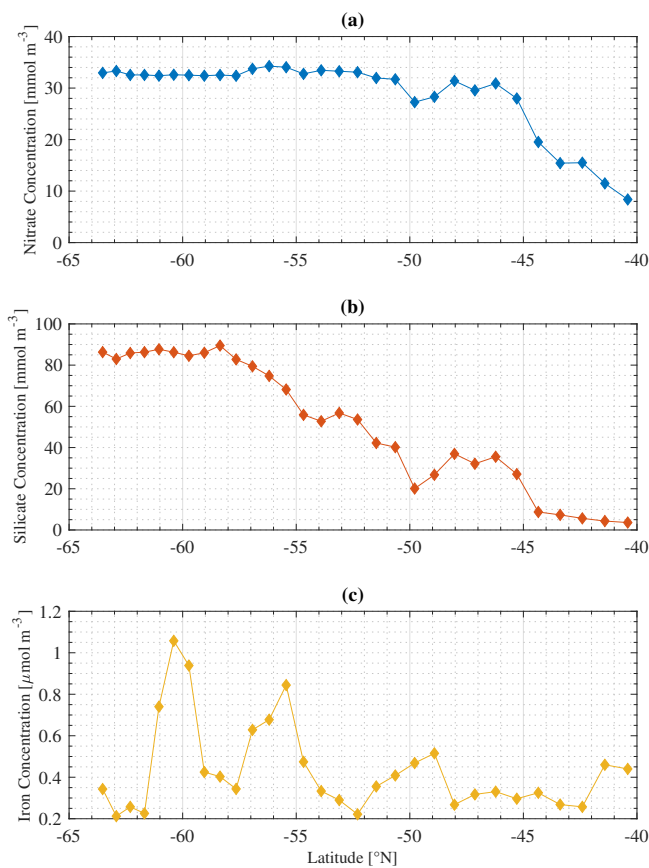
Figure 5. Nitrate (a), silicate (b), and iron (c) lower boundary conditions along the averaged model meridional section

location for the open SO (Louanchi et al., 2001), which is a HNLC region (Tréguer and Jacques, 1992). The KERFIX dataset
is particularly useful because it enables validation of model results, forcings and boundary conditions with observational data
for at least one station of the model: a reasonable comparison at one station increases the trust in the entire model.

The average nitrate concentration at KERFIX as measured between 1992 and 1994 at 300 m depth (the depth at which
5 the boundary condition is defined at station 18) was 31 $mmol\,m^{-3}$. This compares well with the GLODAPv2 boundary
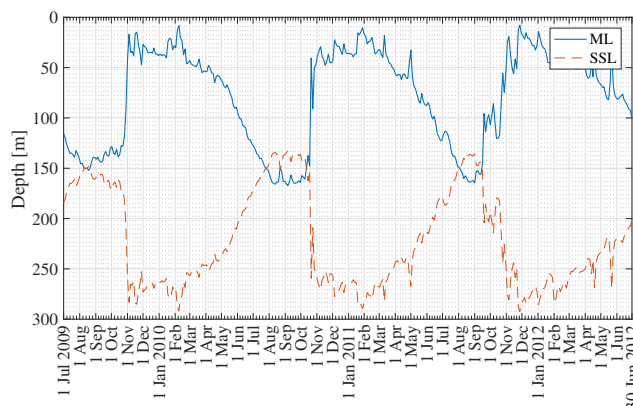
Figure 6. Mixed layer and Subsurface layer thicknesses at station 18 from 1 July 2009 to 30 June 2012

condition for N (Fig. 5 (a)). The average silicate concentration at KERFIX was 39 $mmol\,m^{-3}$ which is again very close to the GLODAPv2 boundary condition for Si (Fig. 5 (b)).

Fig. 6 shows the ML depth from 2 January 2008 to 30 December 2012 at KERFIX based on the $\Delta\rho = 0.03\,kg\,m^{-3}$ density criterion applied to the B-SOSE dataset. The seasonality is clear, with deepest mixed layers in late austral winter (150 - 200

5 m) and shallowest mixed layers in austral summer (50 m). A relatively rapid decrease in ML depth is visible in the second half of October (early austral spring). This is in line with observations at KERFIX between January 1990 and March 1995 (Louanchi et al., 2001). The ML depth is of similar magnitude, and a rapid decrease at the end of October is observed as well. The high-frequency variability is attributed to events of strong re-stratification in austral winter, and de-stratification by storms in austral summer.

10 ## 4 Results

4.1 Inter-annual variability at KERFIX

The permanently open ocean zone is a vast and heterogeneous area in the SO. It is a remote and rough region, and it is thus relatively poorly sampled (Smith et al., 2000). Due to limited data availability, there is no added value in expanding the model with a zonal component; thus, the model represents a zonal average of the SO. Despite the attractive simplicity of

15 this assumption, it makes comparing model results with one localised sampling dataset (obtained during a specific cruise, or satellite mission, acquired at a certain time in year, or using specific methods, etc.) complex. While the model results can be a representative average, localised observational data are not necessarily so. With this caveat, model results at station 18 (the

KERFIX latitude) are compared with the KERFIX observational data between January 1990 and March 1995, with satellite data and with other model results.

Fig. 7 (a) and (b) show the modelled phytoplankton and zooplankton biomass between 1 July 2009 and 30 June 2012 at station 18. Diatoms are the first phytoplankton species to bloom. The peak of 1.4 - 1.6 $mmol\,N\,m^{-3}$ occurs mid-November. A second diatom peak occurs around mid-March, and is significantly smaller than the main diatom bloom, with a concentration up to 0.5 $mmol\,N\,m^{-3}$. Nanophytoplankton biomass reaches a maximum concentration of 0.9 - 1 $mmol\,N\,m^{-3}$ at the beginning of January. Coccolithophores never attain high concentrations. However, just like diatoms and nanophytoplankton they are able to sustain biomass from the beginning of December to the end of May.

The zooplankton biomass closely follows the phytoplankton curves. Mesozooplankton concentration exhibits a bloom shortly after the diatom bloom. Following this bloom mesozooplankton feed on microzooplankton. This factor, together with lower nanophytoplankton and coccolithophore biomass keeps the microzooplankton biomass rather low.

The units of the phytoplankton biomass are converted from $mmol\,N\,m^{-3}$ to $mg\,chl\,a\,m^{-3}$. A Redfield C:N-ratio of 6.625 is used (Redfield, 1934). Gall et al. (2001) investigated the response of the phytoplankton community to in-situ iron fertilisation in the SO waters (SOIREE). One of their findings was that iron availability influenced the carbon to chlorophyll-a ratios. Prior to fertilisation the algal community had a mean carbon to chlorophyll-a ratio < 100 (Diatoms: 94, nanophytoplankton: 40). After fertilisation algal community-mean carbon to chlorophyll-a ratio had decreased to 40. Similarly, temperature, light and nutrient availability affect the carbon to chlorophyll-a ratio (Cloern et al., 1995), which can vary from 100 to 30. Pondaven et al. (2000) used a value of 60 for nanophytoplankton, and 45 for microphytoplankton, in their model study at KERFIX in the Southern Ocean. In our model a carbon to chlorophyll-a ratio of 100 will be used for each phytoplankton species, independent of temperature, light or nutrient concentrations. Note that the chlorophyll-a concentration is inversely proportional with the ratio. So using a ratio of 80 instead of 100 will increase the chlorophyll-a concentration with 25%.

Modelled total chlorophyll-a concentration in the ML between 1 July 2009 and 30 June 2012 is presented in Fig. 7 (c) (solid line), with the dashed line showing assimilated daily chlorophyll-a data from the NASA Ocean Biogeochemical Model (NOBM) (Goddard Modeling and Assimilation Office (GMAO), 2014). Monthly satellite data for chlorophyll-a are marked by triangles (MODISA), and the comparison with in-situ KERFIX data is shown with diamonds. There are some similarities and some discrepancies. Whereas the model finds no biomass in austral winter, the satellite data and NOB model find biomass throughout the year. No blooms are observed in the satellite and NOBM curves. The satellite data is monthly averaged. This can lead to averaging out of possible short blooms. Apart from the difference in austral winter and the lack of a bloom in the NOB model and satellite data, the biomass concentrations in austral summer and autumn are similar. Our model attains reasonable results compared with the in-situ KERFIX data: a phytoplankton peak around mid-November, and low but persistent chlorophyll-a values in summer and autumn. However, as for the satellite data, there is an observed winter concentration of phytoplankton that is not captured by our model.

Pondaven et al. (2000) used a similar 1-D model to calculate the phytoplankton biomass in the ML at KERFIX, using physical forcing between 1 July 1990 and 30 June 1991. They found a bloom of 1.5 $mg\,chl\,a\,m^{-3}$ on 15 November. Their results were compared to actual chlorophyll-a data obtained in 1992, 1993 and 1994 in which peaks of about 0.8 $mg\,chl\,a\,m^{-3}$
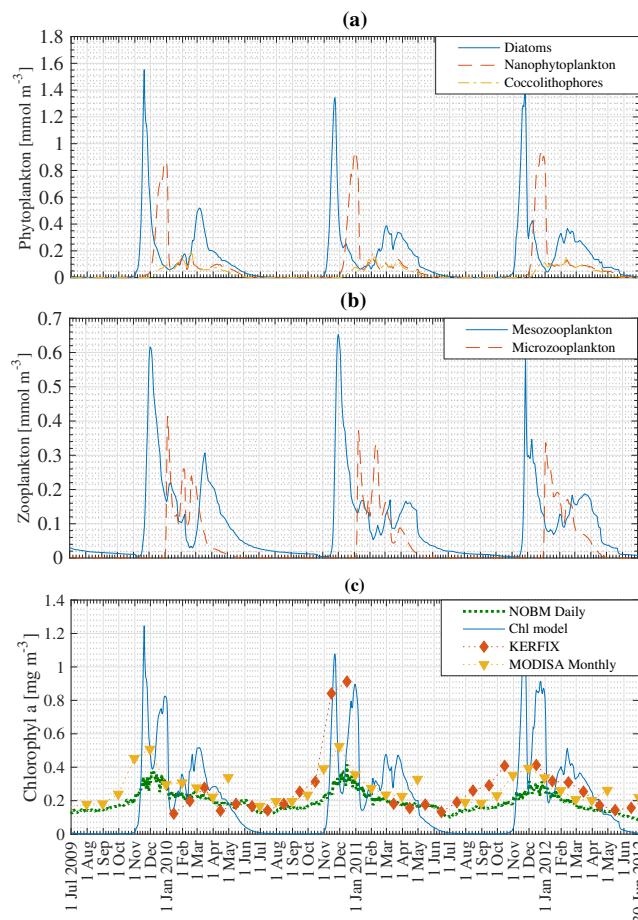
Figure 7. Model result: diatom, nanophytoplankton and coccolithophore concentration (a), mesozooplankton and microzooplankton concentration (b), and chlorophyll-a concentration compared to KERFIX in-situ data (♦), to MODISA satellite data (▼) and to NOBM results (··) (c) in the mixed layer at station 18 from 1 July 2009 to 30 June 2012

were observed. Similarly, Pasquer et al. (2015) used the SWAMCO model at the KERFIX location to find a bloom of about 1.5 $mg\,chl\,a\,m^{-3}$ in spring. However, the bloom lasted significantly longer than found in our model or in the model by Pondaven et al. (2000).

In situ measurements at KERFIX (1991-1995) revealed the occurrence of blooms at that location, despite the absence of blooms in satellite data. Highest recorded in situ values were about 0.8 $mg\,chl\,a\,m^{-3}$. It is possible that due to the monthly frequency of sampling, higher values were missed out. Our modelled peak of 1.5 - 1.6 $mg\,chl\,a\,m^{-3}$ is thus realistic. The only characteristic unique to our model is the zero biomass in austral winter.

5   Fig. 8 (a), (b) and (c) present the modelled nutrient concentrations in the ML. It is important to recall that the period 2009-2012 (in our model) is compared with the period 1993-1995 (in KERFIX). Diamonds denote monthly averaged observations at KERFIX between July 1993 and July 1995. Nutrient levels are high in winter due to entrainment, diffusion and upwelling/advection (the three processes responsible for re-setting winter concentration in the model, although as shown below entrainment is the most important). As soon as diatoms start blooming, nutrients are drawn down rapidly and reach

10   their lowest values during spring/summer, after the nanophytoplankton bloom. The modelled October nitrate concentration is 26 $mmol\,m^{-3}$. Biological utilisation reduces this concentration to 23 $mmol\,m^{-3}$ in May, a decrease of 3 $mmol\,m^{-3}$. During in situ measurements at KERFIX, peak winter concentrations of about 28 $mmol\,m^{-3}$ and summer minima of about 24 $mmol\,m^{-3}$ were observed (Louanchi et al., 2001). The difference between summer and winter is relatively similar between our model results and the in-situ KERFIX data, although of slightly larger amplitude in the data. The overall modelled nitrate

15   cycle compares well with the KERFIX observations too. The modelled October silicate concentration is 20 $mmol\,m^{-3}$. Biological utilisation reduces this concentration to 9 $mmol\,m^{-3}$ by December, a decrease of 11 $mmol\,m^{-3}$. In-situ KERFIX data (Louanchi et al., 2001) showed a winter concentration of about 20 $mmol\,m^{-3}$ and a summer concentration that is about 12 $mmol\,m^{-3}$ lower. Despite the reasonable agreement between these values, there is a clear temporal offset between the model's seasonality and the observed seasonality at KERFIX for Si concentrations. The timing of highest concentration is

20   well modelled, as is the rapid depletion of Si at the start of spring as well. The restoring of Si after the spring bloom is rather different. Observations show absolute minima at a time in which modelled concentrations are recovering. It appears that the model misses the actual Si minimum. This likely means that the diatom bloom is cut off too soon, and that a longer-lasting bloom as found in the model study by Pasquer et al. (2015) is more realistic. Modelled concentrations of the micronutrient iron are low throughout the year. Winter concentrations reach 0.12 $\mu mol\,m^{-3}$. Primary production reduces iron levels to almost

25   zero in summer. Consequently phytoplankton cannot sustain biomass and the modelled concentration of phytoplankton reaches zero. As discussed earlier, this is not in line with observations and other model studies. The reason for this discrepancy might be that remineralisation in the model is underestimated. Tagliabue et al. (2014) suggest that iron concentration is replenished by a boost of entrainment in winter leading to phytoplankton blooms and that a limited amount of iron is sustained throughout the rest of the year by efficient remineralisation, allowing biomass to be sustained. Another explanation for the lack of biomass

30   in winter is the low light availability during large parts of the year. As the model uses an average PAR for the entire ML, it is likely that PAR at the surface is underestimated by the model.

The nanophytoplankton bloom is evidence that there are still sufficient nutrients available in the ML after the diatom bloom. This raises the question of what it is that limits further diatom production. Diatom growth can be limited by insufficient light, significant grazing pressure, Si limitation, or Fe limitation in our model. At that time of the year, it is unlikely that

35   diatom growth is limited by lack of light. According to our model, diatoms are not limited by Si either, as concentrations are
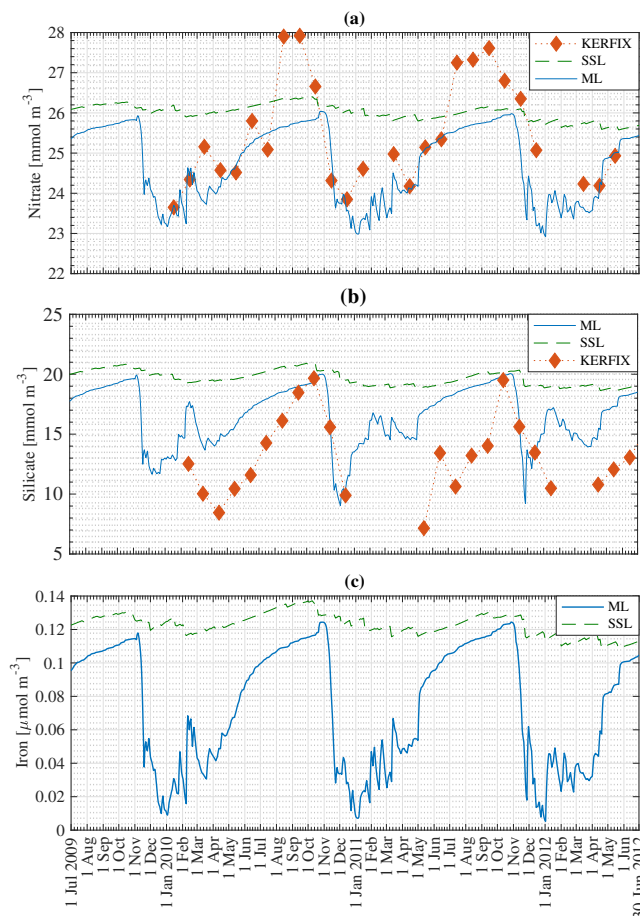
Figure 8. Model result: nitrate (a), silicate (b), and iron (c) concentration in the mixed layer (–) and in the subsurface layer (- -) compared to KERFIX in-situ data (♦) at station 18 from 1 July 2009 to 30 June 2012

sufficiently high throughout the year (Fig. 8 (b)), in line with KERFIX data. This is in contrast with results of the model study by Pondaven et al. (2000), who found that diatoms are prevented from blooming at the surface due to a lack of Si. Their 1-D model (Pondaven et al., 2000) has a high vertical resolution, and is able to capture the vertical structure of nutrient distributions. This explains why their study obtains a silicate concentration as low as 3 $mmol\,m^{-3}$ at the surface. Note also that they use a

relatively high half saturation constant for Si uptake, Si_h, $8\ mmol\,m^{-3}$, which is within the range of measured values (12-27 $mmol\,m^{-3}$ have been reported in the open SO (Caubert, 1998; Jacques, 1983)). While in our model a substantially lower Si_h of $1\ mmol\,m^{-3}$ is adopted, our results are not sensitive to this choice. Indeed, running the model with $Si_h = 8\ mmol\,m^{-3}$ does not change the diatom bloom concentration significantly, indicating that in an averaged ML diatom growth is not limited by

5 insufficient Si. Pondaven et al. (2000) suggest that the high values of the half saturation constant for Si uptake Si_h are actually a consequence of iron limitation, such that their model (which does not explicitly represent Fe) accounts for iron limitation through a high value of Si_h. Si limitation then becomes a consequence of iron limitation. In our model, diatom growth is limited by iron. Nanophytoplankton are capable of assimilating iron more efficiently. However, the mesozooplankton bloom follows the diatom bloom closely, suggesting that intensive grazing limits diatom growth. To substantiate this interpretation,

10 we conduct a model run with reduced grazing pressure in the model (no mesozooplankton); this reveals that diatom growth is indeed limited by a lack of iron. When the iron concentration decreases below $0.05\ \mu mol\,m^{-3}$, the diatom abundance is reduced. The diatom population decreases more rapidly when mesozooplankton are present in the model, but the presence of mesozooplankton does not significantly alter the distribution of phytoplankton over the season. When diatoms disappear, nanophytoplankton use the remaining of the iron until it is depleted to an even lower level where it becomes limiting to them

15 as well. When iron concentrations increase around February - March, diatoms are able to bloom for a second time, albeit in a less pronounced manner.

4.2 Nutrient distribution along an averaged section in the SO

The macronutrient gradient in the upper limb of the SO is reproduced in the model (Fig. 9 (a) and (b)). To generate these figures, winter is defined here as the period (1 July 2010 and 30 June 2011) in which nutrient concentrations in the water are

20 highest, whereas summer is defined as the period (1 July 2010 and 30 June 2011) in which nutrient concentrations are lowest. The winter nitrate concentration at the Southern Boundary ($\sim 60°$S) is about $30\ mmol\,m^{-3}$, decreasing approximately linearly to $24\ mmol\,m^{-3}$ at $45°$S, i.e. a reduction of $6\ mmol\,m^{-3}$ over 15 degrees of latitude ($0.4\ mmol\,m^{-3}$ per degree latitude). From 45 to $40°$S the gradient is stronger, with a reduction of $10\ mmol\,m^{-3}$ over 5 degrees of latitude ($2\ mmol\,m^{-3}$ per degree latitude). The winter nitrate gradient is overall $0.7\ mmol\,m^{-3}$ per degree latitude. The gradient is a lot stronger for silicate

25 (Fig. 9 (b)) . At the Southern Boundary, $70\ mmol\,m^{-3}$ is reached in winter. Concentrations (also in winter) reduce to zero at $40°$S, i.e. a gradient of about $3\ mmol\,m^{-3}$ per degree latitude. These results are in line with observations made along sections in the SO (1 Introduction and Tréguer and Jacques (1992); Pollard et al. (2002); Assmy et al. (2013); Smith et al. (2000); Read et al. (2002)).

Note that the deep nitrate concentration north of $44°$S is lower than the modelled winter/summer nitrate concentrations.

30 Because there are no observational data that support this claim, it seems that the modelled nitrate concentration north of $44°$S is overestimated or that the deep water concentration is underestimated. This should be taken into account when assessing the results north of $44°$S further in this work.

There is no substantial gradient in the iron concentration, irrespective of season (Fig. 9 (c)). The summer gradients for N and Si are similar in shape to the winter gradients. The difference between the summer and winter gradient provides a good

indication of primary productivity at a certain station. For iron, the summer concentration is near-zero all along the section, indicating the limiting nature of the micronutrient in the model. The winter concentration of iron is correlated with the summer concentration of both N and Si. If abundant iron is present, more Si and N can be assimilated, leading to larger differences between summer and winter concentrations of these macronutrients. The dotted line in each of Fig.9 (a), (b) and (c) shows the boundary condition as used in our model. This indicates the existence of a connection between the boundary condition and the ML. In summary: the winter concentration (gradient) of N and Si in the ML depends strongly on the deep water concentration (gradient) of N and Si. The summer concentration of N and Si also depends strongly on the winter concentration of iron, and on the amount of biological production that it enables during the growing season. The model thus suggests that a crucial factor in understanding the observed gradients in surface nutrient concentration is the concentration at depth along a section.

4.3 Processes restoring winter concentrations of N and Si in the mixed layer

Winter nutrient concentrations in the ML are depleted by biology (use of nutrients by phytoplankton and sinking of diatoms and detritus) and restored due to four processes in our model: entrainment, diffusive mixing, remineralisation and advection/upwelling. The absolute contribution of each process to the restoration of nitrate in the ML for station 18 is shown in Fig. 10. Entrainment is found to play the most important role in re-setting the winter concentration of N at station 18. In order to quantify the importance of each process at each station, the relative contribution of each restoring process is calculated. The relative contribution of a process is defined here as the increase of the nutrient N, Si or Fe due to that process between 1 July 2010 and 30 June 2011, divided by the total increase of that nutrient in that period. The first of July is chosen because physical effects are small at that time, as seen in Fig. 10.

The relative contribution of each process is quantified and visualised in Fig. 11 (a) and (b) for N and Si, respectively. Entrainment of water from the SSL to the ML is the dominant process restoring winter N concentrations in the ML: typically about 50 percent, with a peak of up to 80 percent around 48°S. Remineralisation is important as well, providing 20 to 40 percent of the nitrate depending on latitude. Diffusive mixing is of minor importance (about 10 percent). Note that this result justifies the omission of horizontal diffusion in the model. Advection/upwelling is unimportant too. At some latitudes, advection contributes negatively; the concentration of N at 49°S is lower than the concentration at 48°S and for that reason the effect of water flowing northward from 49°S to 48°S is to lower the concentration at 48°S. From about 44°S, advection plays a more important role than entrainment. As explained earlier (Fig. 9 (a)) the concentration in the deep water is lower than that in the ML and SSL. There is a loss of nutrients from the SSL to the deep, and therefore the concentration of the water entrained into the ML is substantially lower and entrainment is reduced. Although advection plays a more important role in that zone, it is noted that the difference between summer and winter concentrations are very small overall, indicating a low primary production compared to stations further south

There are two main findings. First, and most importantly, entrainment is the dominant process restoring N in the ML followed by remineralisation. Diffusive mixing and advection play a minor role. Second, when the concentration in the deep water is low, advection is the dominant process restoring winter concentrations. However, the change in concentration from summer to winter is very limited in this area due to low primary production.
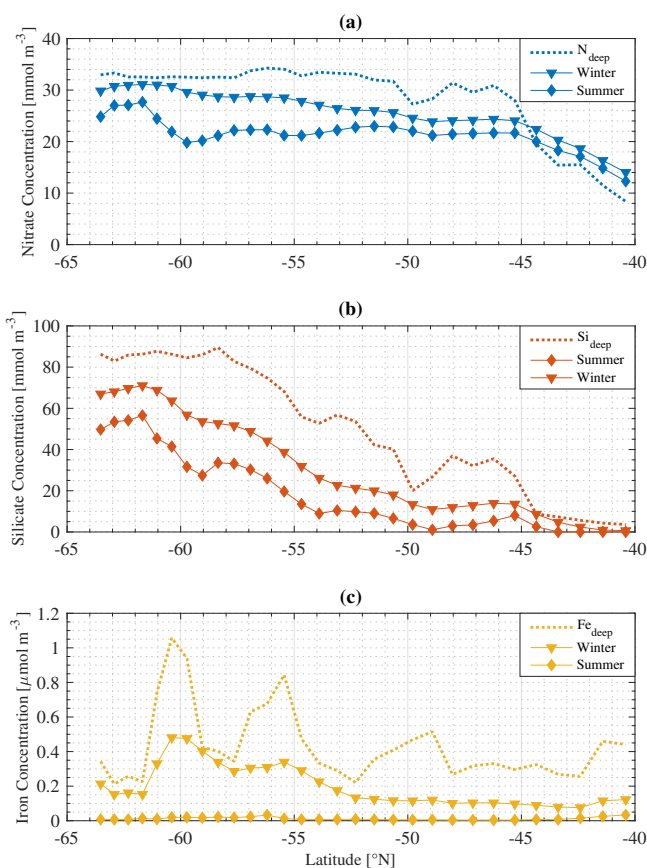
Figure 9. Model result: summer (♦) and winter (▼) nitrate (a), silicate (b), and iron (c) concentration in the mixed layer along the average meridional section compared to the deep water concentration (··)

Entrainment also dominates wintertime recovery of ML silicate levels (Fig. 11 (b)). Diffusive mixing is rather unimportant, as is remineralisation. As there are only two significant processes, it is found that the percentage contribution of advection/upwelling is nearly a replica of the entrainment term.
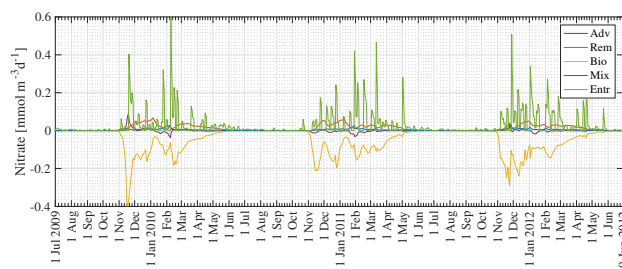
Figure 10. Model result: absolute contribution of advection/upwelling, remineralisation, biology, diffusive mixing and entrainment to the nitrate concentration in the mixed layer

An interesting difference is noticed between N and Si. Remineralisation is not important for Si, yet it is important for N. There are two reasons for this. First, the choice of the model remineralisation parameter is different for Si and N, being twice as high for N as for Si ($0.16\ d^{-1}$ and $0.08\ d^{-1}$, respectively). Second, Si sinks out of the detritus pool much faster than N does, such that less Si gets remineralised from detritus back into the ML. In the model the sinking velocity of N and Fe in detritus is

5   equal to 5 m d^{-1}, while it is chosen as 50 m d^{-1} for Si. These choices are incorporated in our model to represent uncoupling of N and Si export (Tréguer and Jacques, 1992; Pollard et al., 2002; Assmy et al., 2013). Particulate Si (diatom frustules) sinks faster and dissolves at greater depth, or does not dissolve and ends up in the siliceous ooze (Assmy et al., 2013).

Fig. 11 (c) shows the relative contribution of each process to the winter recovery of iron at each station. As for N and Si, entrainment is the most important process restoring the winter concentration. It is about ten times more important than diffusive

10   mixing. This result is in line with a data study by Tagliabue et al. (2014). We see that remineralisation plays an important role as well, despite the fact that it is insufficient to sustain phytoplankton biomass throughout the year.

5   Discussion

5.1   Role of physics in shaping meridional gradients of N and Si in the mixed layer

The observed gradient of N and Si along a south-to-north section is a smooth mirror image of the gradient observed in the

15   boundary conditions for N and Si. This suggests that, if no boundary condition gradient existed, no gradient would be observed in the ML. Indeed, if the model is run with a fixed boundary condition for N ($30\ mmol\,m^{-3}$) and Si ($60\ mmol\,m^{-3}$) along the section, the winter gradient disappears, and winter concentrations of both N and Si are relatively similar along the section (Fig. 12 (a)). This strongly suggests that the observed meridional nutrient gradient in the ML results from the deep-water nutrient distribution. Having a nutrient gradient below the SSL is a necessary requirement for a nutrient gradient to occur close to the

20   surface.
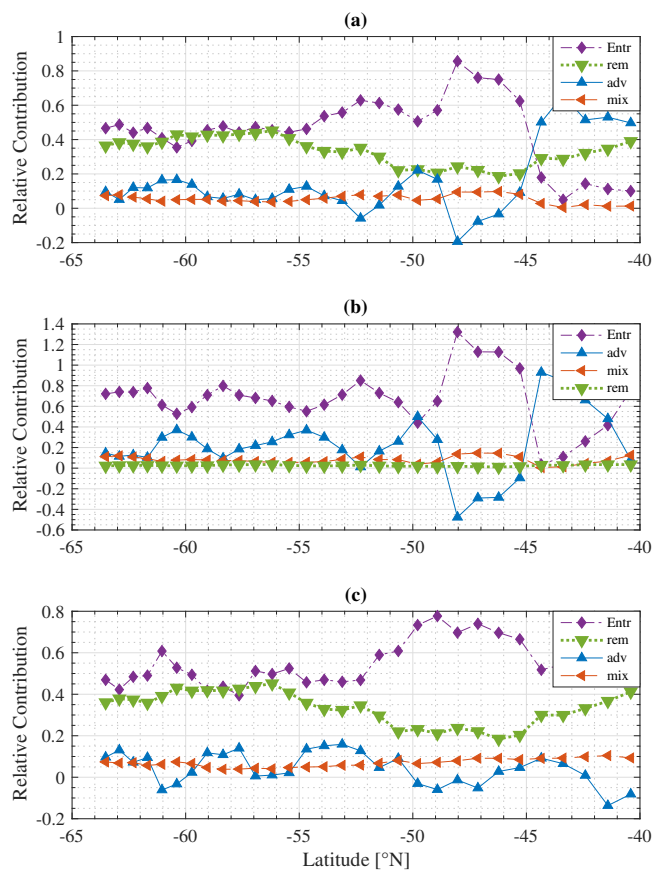
Figure 11. Model result: relative contribution of entrainment (♦), diffusive mixing (◄), remineralisation (▼) and advection/upwelling (▲) to restoration of the winter nitrate (a), silicate (b), and iron (c) concentration at each station along the average meridional section

Results when biology is excluded from the model suggest that biological processes are not necessary to reproduce a near-surface macronutrient gradient. Fig. 12 (b) compares the standard model results with a model run where biology is omitted. While nutrient gradients are less steep than in the standard run, indicating that biology does affect the nutrient distribution as is generally accepted, the gradients are still substantial. Only near the northern end of the model domain, where Si concentrations

are very low, is the influence of biology prominent. Winter concentration of Si in the north is higher when diatoms are excluded from the model.

Surface concentrations are closer to the deep water concentrations as is as expected since biology provides an important sink for nutrients to leave the model. However concentrations do not reach deep water values when biology is excluded from

5 the model which could be expected with entrainment/detrainment isolated as a prominent process. Entrainment/Detrainment is important, but it occurs only from ML to SSL and from SSL to ML. So the total amount of nutrients is divided between SSL and ML (variable with changing ML and SSL depth). The interaction with other boxes is via advection; the interaction with the deep (boundary condition) is via diffusive mixing. Diffusive mixing plays a role, but only on larger timescales, compared to advection and entrainment (k_{mix} rather low). So, ML concentration and SSL concentration are very similar without biology,

10 but to equilibrate with the deep water concentration, the model would have to run for a longer time period.

Fig. 12 (a) and (b) indicate that there would be no ML nutrient gradient at all without a gradient at depth, and without the connection between the deep and surface waters. Fig. 11 (a) and (b) reveal that physical processes prevail in providing this connection. Thus, our model supports the suggestion by Pollard et al. (2002) that entrainment (deep winter mixing) is the main factor controlling the winter concentration of Si and N in the ML. Note that we cannot explicitly demonstrate this by running

15 the model without physics, because iron would not be replenished in winter, phytoplankton and zooplankton would vanish, and N and Si would remain constant, making model results uninformative.

5.2 Different drivers over different timescales

Model results are found to be rather sensitive to changes in C_{deep}, the deep-water nutrient concentration. It is not possible to reproduce the strong Si gradient and weaker N gradient if C_{deep} along the section is assumed constant, at least over the

20 timescales of relevance to the model (i.e. timescales of years to decades over which the deep-water nutrient distribution may be assumed to be constant in time). C_{deep} is, by definition, the concentration at the base of the SSL. If zonal variation in C_{deep} is a necessary requirement for sustaining the nutrient concentration gradient in the ML, and if the ML gradient reflects a deep-water gradient, it is necessary to think about the processes responsible for the deep-water gradient. Our model can address the question of proximate causes of silicate depletion at the northern end of the overturning's upper limb, it can assess the cause

25 of surface silicate patterns over short timescales of years. However, our model provides no insights into the controls over the deep-water gradient on longer timescales. This problem is therefore beyond the scope of this work.

It seems reasonable, however, to assume that biology or, more precisely, the interplay between biology and physics, is key to explaining the observed deep-water macronutrient distribution in the SO over timescales of decades and longer. The overturning supplies nutrients to the ML in the isopycnal layer ρ_1 (Fig. 13). The upwelled water is then transported northward.

30 As the water enters isopycnal ρ_2, its nutrients will be consumed by phytoplankton in summer. After the end of the productive season, organic matter will sink. Some will be remineralised in layer ρ_2, but some will be remineralised in layer ρ_1. Thus, primary production in the ML of layer ρ_2 will eventually provide nutrients not only to layer ρ_2 but also to layer ρ_1. Similarly, organic matter generated in layer ρ_3 will be remineralised in ρ_3, ρ_2 and ρ_1. In this way, a horizontal nutrient gradient at depth can be created.
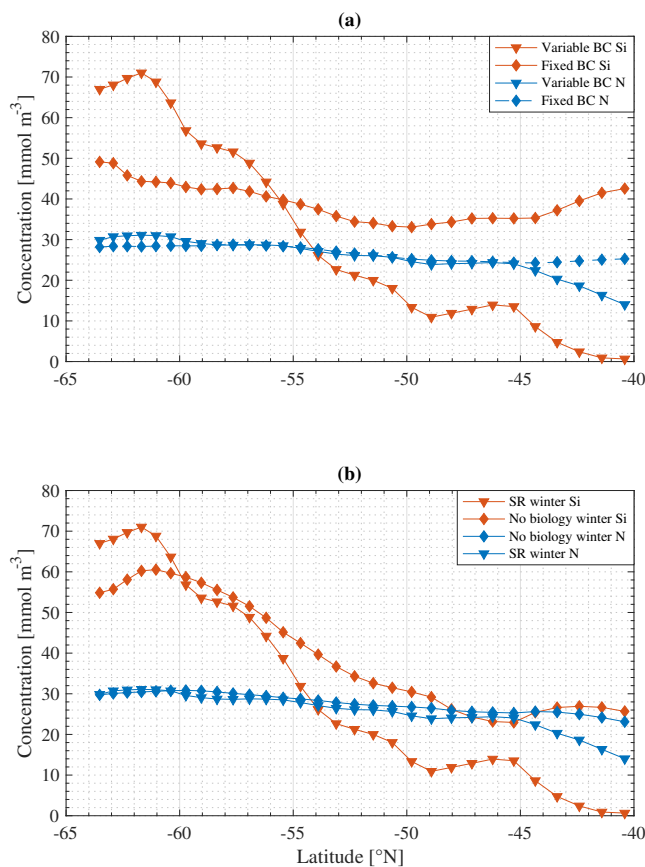
Figure 12. Model result: winter nitrate and silicate concentration in the mixed layer along the average meridional section - a comparison of the standard model run (SR) (▼) with a model run with constant boundary condition (♦) (a) and a model run without biology (♦) (b)

5.3 Robustness of the main result

Some additional model runs were carried out in order to investigate the sensitivity of the main result to some assumptions. Firstly, upwelling velocities were increased by 50% in one model run and decreased by 50% in another. The model does not explicitly model either eddies or Ekman transport and therefore makes no distinction between the different sources of the
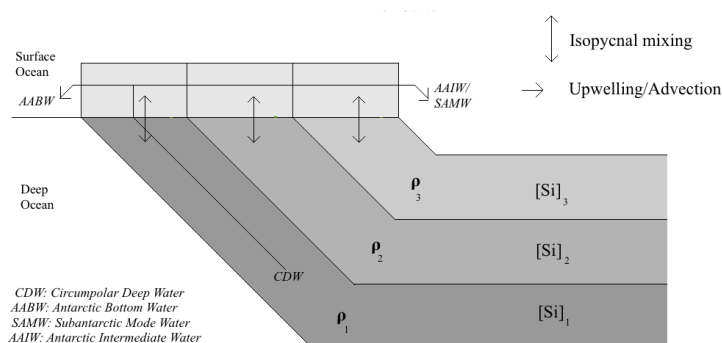
Figure 13. Simplified representation of the banded structure of the Southern Ocean and the consequent nutrient concentrations at depth. Darker shading indicates higher nutrient concentrations

northward transport. The northward transport is calculated from conservation of mass and so depends on upwelling velocities. Therefore, the northward transport was also altered in these runs. It should be kept in mind that these alterations are most likely contradicted by some of the data to constrain the behaviour of the SOSE model.

Secondly, in reality the northwards transport is not completely restricted to the ML but rather takes place partly in the SSL
5 as well. For one model run 80% of the total northward transport was made to occur in the ML and 20% in the SSL.

As shown in Fig. 14, applying these changes one by one to the model does not greatly affect the final result in terms of the primacy of physical processes (entrainment) over biological processes in driving nutrient patterns. For each altered model it remains true that the silicate gradient (the south-to-north gradient in the ML concentration) is more strongly affected by making the bottom boundary condition constant than it is by removing biology from the model.

10 ## 5.4   Model performance

The model has proven to be a useful tool for better understanding the processes responsible for the nutrient distribution along an averaged meridional section in the SO. Nutrient cycles are reproduced with reasonable skill. There is room for improvement when it comes to the Si cycle, but it is not within the scope of this work to produce a completely realistic simulation, and our important results are not affected by this limitation. Phytoplankton cycles are modelled quite well. In reality, blooms might
15 be more spread over the season than in our model, which generates a short and intensive bloom. In reality, non-negligible populations of phytoplankton appear able to survive throughout the SO winter, whereas they die away in the model. However, this discrepancy does not affect our results, given that the large majority of nutrient removal takes place in the spring and summer

A key result of our model study is that winter nutrient concentrations in the ML are closely linked to the deep-water con-
20 centrations. Our model is a box model. Physically more complex models should also be used to examine this problem. The
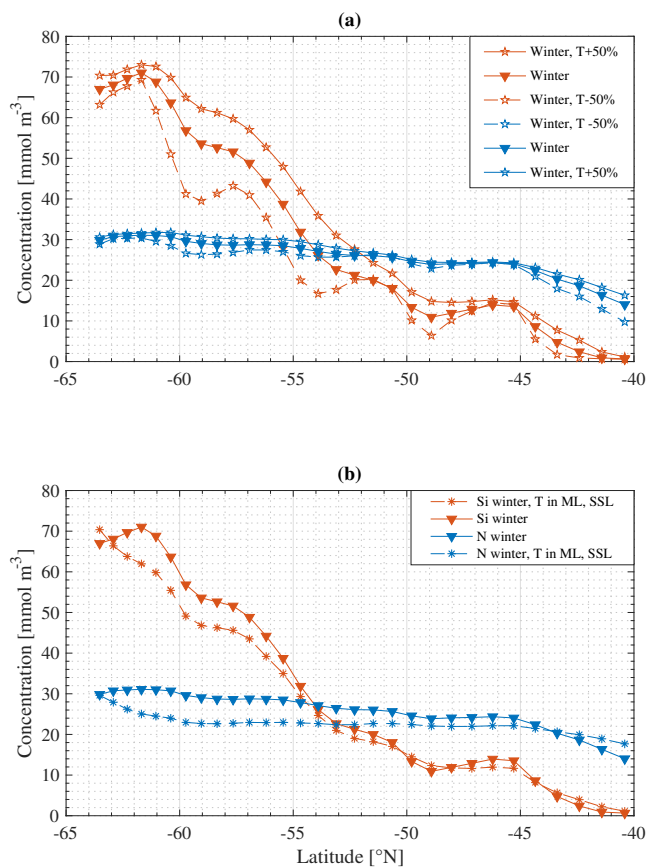
Figure 14. Model result: winter nitrate and silicate concentration in the mixed layer along the average meridional section - a comparison of the standard model run (▼) with a model run where transport is increased and decreased with 50% (∗) (a), and with a model run where transport is divided over the ML and SSL (∗) (b)

use of a SSL in this model is a first step in that direction, but our model lacks the vertical resolution to accurately recreate the vertical profile. At the moment, the model's boundary is defined at the base of the subsurface layer, but the deep ocean is not resolved at all. Future studies should look to reproduce the results obtained here in models with higher spatial resolution and

more complete physics, including GCMs. When doing so, it is important however that the higher resolution models achieve a similar degree of realism in terms of the nutrient fields, plankton ecology and seasonal ML dynamics. A fine-resolution model with unrealistic deep nitrate and silicate concentrations, or unrealistic iron distributions, is likely to give unrealistic results in terms of the question addressed here.

5.5 Implications

This work reveals the importance of winter resetting (because of entrainment) in controlling geographical patterns of surface water chemistry in the SO. While Si:N ratios have been studied here, the principle is likely to apply to other chemical elements, including carbon. Biogeochemical models of, or including, the SO must include the process of entrainment as accurately as possible if they are to hope to reproduce reality.

The SO exerts a far-field influence on productivity in other ocean areas via SAMW. Our results suggest that effects of global change on biology are unlikely to greatly alter SAMW composition on annual to decadal timescales, because biology is of secondary importance on these timescales. However, our results suggest that global change could alter SAMW composition through changes to physics. For instance, increases in westerly wind stress leading to increased upwelling intensity would be expected to force a closer correspondence between surface and deep concentrations. Conversely, if the main effect of global warming were to be an increase in surface water buoyancy (increased stratification), leading to a reduction in the depth of mixing in winter, then surface concentrations would become less strongly coupled to deep values. In this latter scenario, SAMW composition could change on annual to decadal timescales.

6 Conclusions

A novel modelling approach was used to simulate physical and biogeochemical processes affecting nutrient concentrations in SO surface waters as they circulate in the upper limb of the overturning circulation, from the Southern Boundary to the mode water formation regions. Our aim was to determine which processes modify surface waters from being enriched in both nitrate and silicate near the Southern Boundary, to being nitrate-rich but silicate-poor where mode waters form. We concluded that physical processes acting on the deep ocean gradient are a necessary condition for setting the upper ocean gradient, while local surface biology exerts less influence. When biology was turned off, while maintaining the deep gradient, the model still reproduced a strong Si gradient. Observational data indicate that the nitrate and silicate patterns in surface waters mirror those in deeper waters. Indeed, if the deep-water concentration of macronutrients were fixed at a constant value along the section, the model failed to reproduce a surface gradient. The decline in silicate therefore appears to be driven from below, rather than from within, at least over timescales of years to decades. upper limb (Fig. 2) of the SO overturning circulation modify the water properties of surface waters subducting in the SAMW formation sites. Properties acquired by these water during their time at the surface in the SO thus exert an important influence on the biogeochemistry of many upwelling regions elsewhere in the global ocean.

Code and data availability. B-SOSE is a model-generated best fit to SO observations - an observationally constrained solution to the MIT general circulation model. The data are available at *http://sose.ucsd.edu*.

The Global Ocean Data Analysis Project version 2 (GLODAPv2) (Olsen et al., 2016) contains data of about one million seawater samples from all over the worlds ocean, collected during almost 800 cruises between 1972 and 2013. The data are available at *https://www.glodap.info*.

5 The GEOTRACES first intermediate data product is a platform providing data from cruises around the world (Mawji and et al., 2015) The data are available at *https://www.bodc.ac.uk/geotraces/data/idp2017/*

Cloud cover data is obtained from the NCEP/NCAR 40-year reanalysis project The data are available at *https://www.esrl.noaa.gov/psd/data/gridded/data*

The biogeochemical model is available on request.

Appendix A: Model equations

10 *Diatoms:*

$$\frac{dD}{dt} = \mu_D D - m_D D - G_{MZD} - \frac{v_D}{MLD}D - \frac{k_{mix}}{MLD}D \tag{A1}$$

Nanophytoplankton:

$$\frac{dP_f}{dt} = \mu_{Pf} P_f - m_{Pf} P_f - G_{ZPf} - \frac{k_{mix}}{MLD}P_f \tag{A2}$$

Coccolithophores:

15 $$\frac{dP_c}{dt} = \mu_{Pc} P_c - m_{Pc} P_c - G_{ZPc} - \frac{k_{mix}}{MLD}P_c \tag{A3}$$

Microzooplankton:

$$\frac{dZ}{dt} = \beta(G_{ZPc} + G_{ZPf}) - G_{MZZ} - m_Z Z - \frac{k_{mix}}{MLD}Z \tag{A4}$$

Mesozooplankton:

$$\frac{dMZ}{dt} = \beta(G_{MZD} + G_{MZZ}) - G_{MZZ} - \frac{m_{MZ}MZ}{1+MZ}MZ - \frac{k_{mix}}{MLD}MZ \tag{A5}$$

20 *Grazing microzooplankton:*

$$G_{ZPc} = \frac{g_Z\left(\frac{P_c^n}{K_Z^n}\right)}{1+\frac{P_c^n}{K_Z^n}+\frac{P_f^n}{K_Z^n}}Z \tag{A6}$$

$$G_{ZPf} = \frac{g_Z\left(\frac{P_f^n}{K_Z^n}\right)}{1+\frac{P_c^n}{K_Z^n}+\frac{P_f^n}{K_Z^n}}Z \tag{A7}$$

Grazing mesozooplankton:

25 $$G_{MZD} = \frac{g_{MZ}\left(\frac{D^n}{K_{MZ}^n}\right)}{1+\frac{D^n}{K_{MZ}^n}+\frac{Z^n}{K_{MZ}^n}}MZ \tag{A8}$$

$$G_{MZD} = \frac{g_{MZ}\left(\frac{Z^n}{K_{MZ}^n}\right)}{1 + \frac{D^n}{K_{MZ}^n} + \frac{Z^n}{K_{MZ}^n}} MZ \tag{A9}$$

Attached coccoliths:

$$\frac{dL_a}{dt} = \rho_{CN} C_{max} \psi P_c - \frac{G_{ZPc}}{P_c} L_a - m_{pc} L_a - \frac{k_{mix}}{MLD} L_a - DETACH \tag{A10}$$

5   *Free coccoliths:*

$$\frac{dL_f}{dt} = 0.5\frac{G_{ZPc}}{P_c} L_a - 0.5\frac{G_{ZPc}}{P_c} L_f + m_{pc} L_a - \frac{k_{mix}}{MLD} L_f - \theta L_f + DETACH \tag{A11}$$

DETACH:

$$DETACH = max\left(L_a - \Pi_{max}\frac{C_{cal}}{C_{org}}\rho_{CN}, DR_{min}L_a\right) \tag{A12}$$

Nitrate ML:

$$\frac{dN}{dt} = -\mu_D D - \mu_{Pf} P_f - \mu_{Pc} P_c + m_{Dt_N} Dt_N + \frac{k_{mix}}{MLD}(N^* - N)$$
$$+ \frac{Q_{adv,in} N_{i-1}}{MLD \times A} - \frac{Q_{adv,out} N}{MLD \times A} + \frac{Q_{upw} N^*}{MLD \times A} \tag{A13}$$

Nitrate SSL:

$$\frac{dN^*}{dt} = m_{Dt_N} Dt_N^* + \frac{k_{mix}}{SSLD}(N_{deep} - N^*) - \frac{k_{mix}}{SSLD}(N^* - N) + \frac{Q_{upw}(N_{deep} - N^*)}{SSLD \times A} \tag{A14}$$

Silicate ML:

$$\frac{dSi}{dt} = -\mu_D D \rho_{SiN} + m_{Dt_{Si}} Dt_{Si} + \frac{k_{mix}}{MLD}(Si^* - Si) + \frac{Q_{adv,in} Si_{i-1}}{MLD \times A} - \frac{Q_{adv,out} Si}{MLD \times A} + \frac{Q_{upw} Si^*}{MLD \times A} \tag{A15}$$

Silicate SSL:

$$\frac{dSi^*}{dt} = m_{Dt_{Si}} Dt_{Si}^* + \frac{k_{mix}}{SSLD}(Si_{deep} - Si^*) - \frac{k_{mix}}{SSLD}(Si^* - Si) + \frac{Q_{upw}(Si_{deep} - Si^*)}{SSLD \times A} \tag{A16}$$

Iron ML:

$$\frac{dFe}{dt} = \rho_{FeN}(-\mu_D D - \mu_{Pf} P_f - \mu_{Pc} P_c) + \frac{m_{Dt_N} Dt_N}{\rho_{FeN}} + \frac{k_{mix}}{MLD}(Fe^* - Fe) + \frac{Q_{adv,in} Fe_{i-1}}{MLD \times A}$$

$$- \frac{Q_{adv,out} Fe}{MLD \times A} + \frac{Q_{upw} Fe^*}{MLD \times A} \tag{A17}$$

Iron SSL:

$$\frac{dFe^*}{dt} = \frac{m_{Dt_N} Dt_N^*}{\rho_{FeN}} + \frac{k_{mix}}{SSLD}(Fe_{deep} - Fe^*) - \frac{k_{mix}}{SSLD}(Fe^* - Fe) + \frac{Q_{upw}(Fe_{deep} - Fe^*)}{SSLD \times A} \tag{A18}$$

Detritus (N) ML:

$$\frac{dDt_N}{dt} = m_D D + m_{Pf} P_f + m_{Pc} P_c + m_Z Z + \frac{m_{MZ} MZ}{1 + MZ} MZ + (1-\beta)(G_{ZPf} + G_{ZPc})$$

$$+ (1-\beta)(G_{MZD} + G_{MZZ}) - m_{Dt_N} Dt_N + \frac{k_{mix}}{MLD}(Dt_N^* - Dt_N) - \frac{v_{Dt_N}}{MLD} Dt_N \tag{A19}$$

Detritus (N) SSL:

$$5 \quad \frac{dDt_N^*}{dt} = -m_{Dt_N} Dt_N^* + \frac{k_{mix}}{SSLD}(Dt_N - Dt_N^*) - \frac{k_{mix}}{SSLD} Dt_N^* + \frac{v_{Dt_N}}{SSLD}(Dt_N - Dt_N^*) \tag{A20}$$

Detritus (Si) ML:

$$\frac{dDt_{Si}}{dt} = \rho_{SiN} m_D D + \rho_{SiN}(1-\beta) G_{MZD} - m_{Dt_{Si}} Dt_{Si} - \frac{k_{mix}}{MLD}(Dt_{Si} - Dt_{Si}^*) - \frac{v_{Dt_{Si}}}{MLD} Dt_{SI} \tag{A21}$$

Detritus (Si) SSL:

$$\frac{dDt_{Si}^*}{dt} = -m_{Dt_{Si}} Dt_{Si}^* + \frac{k_{mix}}{SSLD}(Dt_{Si} - Dt_{Si}^*) - \frac{k_{mix}}{SSLD} Dt_{Si}^* + \frac{v_{Dt_{Si}}}{SSLD}(Dt_{Si} - Dt_{Si}^*) \tag{A22}$$

Competing interests. We declare that there are no competing interests present.

References

Anderson, R. F., Ali, S., Bradtmiller, L. I., Nielsen, S. H. H., Fleisher, M. Q., Anderson, B. E., and Burckle, L. H.: WInd-driven upwelling in the Southern Ocean and the deglacial rise in atmospheric CO_2, Science, 323, 1443–1448, 2009.

Assmy, P., Smetacek, V., Montresor, M., Klaas, C., Henjes, J., Strass, V. H., Arrieta, J. M., Bathmann, U., Berg, G. M., Breitbarth, E.,
5   Cisewski, B., Friedrichs, L., Fuchs, N., Gerhard, J. H., Jansen, S., Krägefsky, S., Latasa, M., Peeken, I., Röttgers, R., Scharek, R., Schüller, S. E., Steigenberger, S., Webb, A., and Wolf-Gladrow, D.: Thick-shelled, grazer-protected diatoms decouple ocean carbon and silicon cycles in the iron-limited Antarctic Circumpolar Current, Proceedings of the National Academy of Sciences, 110, 20 633–20 638, 2013.

Brzezinski, M. A.: The Si:C:N ratio of marine diatoms: interspecific variability and the effect of some environmental variables, Journal of Phycology, 21, 347–357, 1985.

10   Brzezinski, M. A., Pride, C. J., Franck, V. M., Sigman, D. M., Sarmiento, J. L., Matsumoto, K., Gruber, N., Rau, G. H., and Coale, K. H.: A switch from $Si(OH)_4$ to NO_3^- depletion in the glacial Southern Ocean, Geophysical research letters, 29, 2002.

Caubert, T.: Le cycle du silicium dans le secteur Indien de L'Ocean Austral., Ph.D. thesis, Université de Bretagne, 1998.

Cloern, J. E., Grenz, C., and Vidergar-Lucas, L.: An empirical model of the phytoplankton chlorophyll:carbon ratio - the conversion factor between productivity and growth rate, Limnology and Oceanography, 40, 1313–1321, 1995.

15   de Boyer Montégut, C., Madec, G., Fischer, A. S., Lazar, A., and Iudicone, D.: Mixed layer depth over the global ocean: An examination of profile data and a profile-based climatology, Journal of geophysical research, 109, 2004.

Deacon, G. E. R.: Physical and biological zonation in the Southern Ocean, Deep-Sea Research I, 29, 1–15, 1982.

Evans, D. G., Zika, J. D., Naveiro Garabato, A. C., and Nurser, A. J. G.: The imprint of Southern Ocean overturning on seasonal water mass variability in Drake Passage, Journal of geophysical research: oceans, pp. 7987–8010, 2014.

20   Fasham, M. J. R.: Variations in the seasonal cycle of biological production in subarctic oceans: A model sensitivity analysis, Deep-Sea Research I, 42, 1111–1149, 1995.

Gall, M. P., Boyd, P., Hall, J., Safi, K. A., and Chang, H.: Phytoplankton processes. Part 1: Community structure during the Southern Ocean Iron RElease Experiment (SOIREE), Deep-Sea Research II, 48, 2551–2570, 2001.

Garrett, C.: Mixing in the ocean interior, Dynamics of Atmospheres and Oceans, 3, 239–265, 1979.

25   Goddard Modeling and Assimilation Office (GMAO): NASA Ocean Biogeochemical Model assimilation ESRID data global daily 0.67x1.25 degrees, Greenbelt, MD, USA, 2014.

Ho, T. Y., Quigg, A., Finkel, Z. V., Milligan, A. J., Wyman, K., Falkowski, P. G., and Morel, F. M. M.: The elemental composition of some marine phytoplankton, J. phycol., 39, 1145–1159, 2003.

Holzer, M., Primeau, F. W., DeVries, T., and Matear, R. J.: The Southern Ocean silicon trap: data-constrained estimates of regenerated silicic
30   acid, trapping efficiencies, and global transport paths, Journal of geophysical research: oceans, 119, 313–331, 2014.

Jacques, G.: Some ecophysiological aspects of the Antarctic phytoplankton, Polar Biology 2, pp. 27–33, 1983.

Jeandel, C., Ruiz-Pino, D., Gjata, E., Poisson, A., Brunet, C., Charriaud, E., Dehairs, F., Delille, D., Fiala, M., Fravalo, C., Miquel, J. C., Park, Y.-H., Pondaven, P., Quéguiner, B., Razouls, S., Shauer, B., and Tréguer, P.: KERFIX, a time-series station in the Southern Ocean: a presentation, Journal of Marine Systems, 17, 555–569, 1998.

35   Kalnay, E., Kanamitsu, M., Kistler, R., Collins, W., Deaven, D., Gandin, L., Iredell, M., Saha, S., White, G., Woollen, J., Zhu, Y., Leetmaa, A., and Reynolds, R.: The NCEP/NCAR 40-year reanalysis project, Bulletin of American meteorological society, 77, 437–470, 1996.

Kirk, J. T. O.: Light and photosynthesis in aquatic ecosystems, Cambridge university press, New York, 2nd edn., 1994.

Louanchi, F., Ruiz-Pino, D., Jeandel, C., Brunet, C., Schauer, B., Masson, A., Fiala, M., and Poisson, A.: Dissolved inorganic carbon, alkalinity, nutrient and oxygen seasonal and interannual variations at the Antarctic Ocean JGOFS-KERFIX site, Deep-Sea Research I, 48, 1581–1603, 2001.

Martin, J. H., Fitzwater, S. E., and Gordon, R. M.: Iron deficiency limits phytoplankton growth in Antarctic waters, Global biogeochemical cycles, 40, 5–12, 1990.

Mawji, E. and et al.: The Geotraces Intermediate Data Product 2014, Marine Chemistry, 2015.

Mazloff, M. R. and National Center for Atmospheric Research Staff: The climate data guide: Southern Ocean State Estimation (SOSE), https://climatedataguide.ucar.edu/climate-data/southern-ocean-state-estimate-sose, 2016.

Merico, A., Tyrrell, T., Lessard, E. J., Oguz, T., Stabeno, P. J., Zeeman, S. I., and Whitledge, T. E.: Modelling phytoplankton succession on the Bering Sea shelf: role of climate influences and trophic interactions in generating Emiliana huxleyi blooms 1997-2000, Deep-Sea Research I, 51, 1803–1826, 2004.

Merico, A., Tyrrell, T., and Cokacar, T.: Is there any relationship between phytoplankton seasonal dynamics and the carbonate system?, Journal of Marine Systems, 59, 120–142, 2006.

Merlivat, L., Boutin, J., and Antoine, D.: Roles of biological and physical processes in driving seasonal air-sea CO_2 flux in the Southern Ocean: New insights from CARIOCA pCO_2, Journal of Marine Systems, 147, 9–20, 2015.

Morrison, A., Frölicher, T., and Sarmiento, J.: Upwelling in the Southern Ocean, Physics Today, 68, 2015.

Oguz, T. and Merico, A.: Factors controlling the summer Emiliania huxleyi bloom in the Black Sea: A modeling study, Journal of Marine Systems, 59, 173–188, 2006.

Olsen, Key, R., van Heuven, S., Lauvset, S. K., velo, A., Lin, X., Schirnick, C., Kozyr, A., Tanhua, T., Hoppema, M., Jutterström, S., Steinfeldt, R., Jeansson, E., Ishii, M., Pérez, F. F., and Suzuki, T.: The Global Ocean Data Analysis Project version 2 (GLODAPv2) - an internally consistent data product for the world ocean, Earth Syst. Sci. Data, 8, 297–323, 2016.

Palter, J., Sarmiento, J. L., Gnanadesikan, A., Simeon, J., and Slater, D.: Fueling export production: nutrient return pathways from the deep ocean and their dependence on the Meridional Overturning Circulation, Biogeosciences, 7, 3549–3568, 2010.

Pasquer, B., Metzl, N., Goosse, H., and Lancelot, C.: What drives the seasonality of air-sea CO_2 fluxes in the ice-free zone of the Southern Ocean: A 1D coupled physical-biogeochemical model approach, Marine Chemistry, 177, 554–565, 2015.

Pollard, R. T., Lucas, M. I., and Read, J. F.: Physical controls on biogeochemical zonation in the Southern Ocean, Deep-Sea Research II, 49, 3289–3305, 2002.

Pondaven, P., Fravalo, C., Ruiz-Pino, D., Tréguer, P., Quéguiner, B., and Jeandel, C.: Modelling the silica pump in the Permanently Open Ocean Zone of the Southern Ocean, Journal of Marine Systems, 17, 587–619, 1998.

Pondaven, P., Ruiz-Pino, D., Fravalo, C., Tréguer, P., and Jeandel, C.: Interannual variability of Si and N cycles at the time-series station KERFIX between 1990 and 1995 - a 1-D modelling study, Deep-Sea Research I, 47, 223–257, 2000.

Read, J. F., Pollard, R. T., and Bathmann, U.: Physical and biological patchiness of an upper ocean transect from South Africa to the ice edge near the Greenwich Meridian, Deep-Sea Research II, 49, 3713–3733, 2002.

Redfield, A.: On the proportions of organic derivatives in sea water and their relation to the composition of Plankton, James Johnstone Memorial Volume, University Press of Liverpool, pp. 176–192, 1934.

Sarmiento, J., Gruber, N., Brzezinski, M. A., and Dunne, J. P.: High-latitude controls of thermocline nutrients and low latitude biologial productivity, Nature, 427, 56–60, 2004.

Smetacek, V., Assmy, P., and Henjes, J.: The role of grazing in structuring Southern Ocean pelagic ecosystems and biogeochemical cycles, Antarctic Science, 16, 541–558, 2004.

Smith, W. O., Anderson, R. F., Moore, J. K., Codispoti, L. A., and Morrison, J. M.: The US Southern Ocean Joint Global Ocean Flux Study: an introduction to AESOPS, Deep-Sea Research II, 47, 3073 – 3093, 2000.

5 Tagliabue, A., Mtshali, T., Aumont, O., Bowie, A. R., Klunder, M. B., Roychoudhury, A. N., and Swart, S.: A global compilation of dissolved iron measurements: focus on distributions and processes in the Southern Ocean, Biogeosciences, 9, 2333–2349, 2012.

Tagliabue, A., Sallée, J.-B., Bowie, A. R., Lévy, M., Swart, S., and Boyd, P.: Surface-water iron supplies in the Southern Ocean sustained by deep winter mixing, Nature Geoscience, 7, 314–320, 2014.

Talley, L. D., Pickard, G. L., Emery, W. J., and Swift, J. H.: Descriptive Physical Oceanography, an introduction, Elsevier, sixth edn., 2011.

10 Taylor, A. H. and Joint, I.: A steady-state analysis of the 'microbial loop' in stratified systems, Marine Ecology Progress Series, 59, 1–17, 1990.

Taylor, A. H., Watson, A. J., Ainsworth, M., Robertson, J. E., and Turner, D. R.: A modelling investigation of the role of phytoplankton in the balance of carbon at the surface of the North Atlantic, Global biogeochemical cycles, 5, 151–171, 1991.

Taylor, A. H., Harbour, D. S., Harris, R. P., Burkill, P. H., and Edwards, E. S.: Seasonal succession in the pelagic ecosystem of the North

15 Atlantic and the utilization of nitrogen, Journal of Plankton Research, 15, 875–891, 1993.

Timmermans, K., van der Wagt, B., and De Baar, H. J. W.: Growth rates, half-saturation constants, and silicate, nitrate, and phosphate depletion in relation to iron availability of four large, open-ocean diatoms from the Southern Ocean, Limnology and Oceanography, 49, 2141–2151, 2004.

Tréguer, P. and Jacques, G.: Dynamics of nutrients and phytoplankton, and fluxes of carbon, nitrogen and silicon in the Antarctic Ocean,

20 Polar Biology, 12, 149–162, 1992.

Twining, B. S., Baines, S. B., and Fisher, N. S.: Element stoichiometries of individual plankton cells collected during the Southern Ocean Iron Experiment (SOFeX), Limnology and Oceanography, 49, 2115–2128, 2004.

Tyrrell, T. and Taylor, A. H.: A modelling study of Emiliania huxleyi in the NE Atlantic, Journal of Marine Systems, 9, 83–112, 1996.

Verdy, A. and Mazloff, M. R.: A coupled physical-biogeochemical data assimilation model for estimating the Southern Ocean carbon system.

25 Submitted to JGR, 2016.

Table 2. Model parameters

Parameter	Symbol [unit]	Diatoms	Nanophytoplankton	Coccolithophores
Max. growth rate	$\mu_{max}\ [d^{-1}]$	1.9	1.4	1.8
Mortality	$m\ [d^{-1}]$	0.045	0.1	0.1
Half sat. constant light	$I_h\ [W\,m^{-2}]$	32.85	32.85	66
Half sat. constant nitrate	$N_h\ [mmol\,m^{-3}]$	0.3	0.3	0.3
Half sat. constant silicate	$Si_h\ [mmol\,m^{-3}]$	1	n.a.	n.a.
Half sat. constant Iron	$Fe_h\ [\mu mol\,m^{-3}]$	0.16	0.06	0.05
Sinking velocity	$v\ [m\,d^{-1}]$	1.5	0	0
Element ratio Si:N	ρ_{SiN}	Eq.11	n.a.	n.a.
Element ratio N:Fe	ρ_{NFe}	Eq.10	Eq.10	Eq.10
C:Chlorophyll-a ratio	$\rho_{C:Chl}\ [mgC\,/\,mgChl]$	100	100	100

Parameter	Symbol [unit]	Microzooplankton	Mesozoopolankton
Grazing rate	$g\ [d^{-1}]$	2.5	1
Mortality	$m\ [d^{-1}]$	0.1	0.2
Half sat. constant food uptake	$K\ [mmol\,m^{-3}]$	1	1
Assimilation efficiency	β	0.75	0.75

Parameter	Symbol [unit]	N / Fe	Si
Remineralisation rate	$m_{Dt}\ [d^{-1}]$	0.16	0.08
Sinking velocity	$v_{Dt}\ [m\,d^{-1}]$	5	50

Parameter	Symbol [unit]	Value
Max. calcification rate	$C_{max}\ [mg\,calcite\,C\,per\,mg\,org.\,C\,d^{-1}]$	1
Half sat. constant light	$I_{H,cal}\ [W\,m^{-2}]$	8.76
Dissolution rate of $CaCO_3$	$\theta\ [d^{-1}]$	0.05
Max. coccoliths allowed per cell	$\Pi_{max}\ [cocc.\,cell^{-1}]$	30
Min. rate of detachment	$DR_{min}\ [d^{-1}]$	0.1
Inorganic carbon content of coccolith	$C_{cal}\ [gC\,coccolith^{-1}]$	0.25×10^{-12}
Organic carbon content of coccolithophore cell	$C_{org}\ [gC\,cell^{-1}]$	10×10^{-12}